Title

Wedge-shaped slice-selective adiabatic inversion pulse for controlling temporal width of bolus in pulsed arterial spin labeling

Journal

Magnetic Resonance in Medicine, 76(3)

ISSN

0740-3194

Authors

Guo, Jia
Buxton, Richard B
Wong, Eric C

Publication Date

2016-09-01

DOI

10.1002/mrm.25989

Peer reviewed

HHS Public Access

Author manuscript

Magn Reson Med. Author manuscript; available in PMC 2017 September 01.

Published in final edited form as:

Magn Reson Med. 2016 September ; 76(3): 838–847. doi:10.1002/mrm.25989.

Wedge-shaped slice-selective adiabatic inversion pulse for controlling temporal width of bolus in pulsed arterial spin labeling

Jia Guo[1,*], **Richard B. Buxton**[1], and **Eric C. Wong**[1,2]

[1]Department of Radiology, University of California, San Diego, La Jolla, California, USA

[2]Department of Psychiatry, University of California, San Diego, La Jolla, California, USA

Abstract

Purpose—In pulsed arterial spin labeling (PASL) methods, arterial blood is labeled via inverting a slab with uniform thickness, resulting in different temporal widths of boluses in vessels with different flow velocities. This limits the temporal resolution and signal-to-noise ratio (SNR) efficiency gains in PASL-based methods intended for high temporal resolution and SNR efficiency, such as Turbo-ASL and Turbo-QUASAR.

Theory and Methods—A novel wedge-shaped (WS) adiabatic inversion pulse is developed by adding in-plane gradient pulses to a slice-selective (SS) adiabatic inversion pulse to linearly modulate the inversion thicknesses at different locations while maintaining the adiabatic properties of the original pulse. A hyperbolic secant (HS) based WS inversion pulse was implemented. Its performance was tested in simulations, phantom and human experiments, and compared to an SS HS inversion pulse.

Results—Compared to the SS inversion pulse, the WS inversion pulse is capable of inducing different inversion thicknesses at different locations. It can be adjusted to generate a uniform temporal width of boluses in arteries at locations with different flow velocities.

Conclusion—The WS inversion pulse can be used to control the temporal widths of labeled boluses in PASL experiments. This should benefit PASL experiments by maximizing labeling duty cycle, and improving temporal resolution and SNR efficiency.

Keywords

Arterial spin labeling; Pulsed ASL; Slice-selective adiabatic inversion; Wedge-shaped adiabatic inversion; Temporal width of bolus

Introduction

Arterial spin labeling (ASL) is an MRI method to measure tissue perfusion non-invasively and has started to become a standard clinical tool for measuring cerebral blood flow (CBF) (1,2). The ASL signal is the difference between two measurements of the signal from a

[*]Correspondence to: Jia Guo, Ph.D. UCSD Center for Functional MRI, 9500 Gilman Drive, MC 0677, La Jolla, CA 92093-0677, jguo@ucsd.edu.

voxel: one in which the longitudinal magnetization of the arterial blood delivered to the voxel is relaxed (control state), and one in which that magnetization has been previously inverted (labeled state). The signal from static spins subtracts out, so the ASL signal is proportional to the amount of delivered arterial blood during a defined time interval. The temporal width of the bolus of blood delivered in the two states must be matched, and in practice there are substantial delays when the blood delivered to the voxel is in neither the control nor the labeled state. The labeling duty cycle and the signal-to-noise ratio (SNR) efficiency (3) of ASL are maximized when all the blood delivered is contributing to the ASL signal, i.e., is either in the labeled or the control states. In continuous labeling methods, including continuous ASL (CASL) (4,5) and pseudo-continuous ASL (PCASL) (6), the blood is labeled as it flows through a labeling plane, allowing for the generation of boluses with a uniform temporal width across vessels that is equal to the labeling duration. However, because labeling cannot be performed during imaging, CASL/PCASL methods leave a considerable portion of blood not contributing to the ASL signal, therefore resulting in sub-optimal labeling duty cycle. In contrast, typical pulsed ASL (PASL) methods (7-10) invert a proximal slab of tissue and the blood within it in a negligible labeling duration, creating boluses of considerably longer temporal widths that can be comparable to or longer than the imaging time. This gives the PASL-based methods the potential to put all the delivered blood in either labeled or control states, leading to the optimal/maximized labeling duty cycle. In applications of ASL where the dynamics of the blood flow are of interest, such as functional MRI (fMRI), high temporal resolution is also desired. In CASL/PCASL, the labeling duration is typically long, resulting in reduced temporal resolution. In comparison, as noted above, the labeling time is negligible in PASL, allowing for a higher temporal resolution, although the SNR in a single label/control pair is lower than that of CASL/PCASL in a typical experimental setting.

Methods to improve the SNR efficiency and temporal resolution of ASL include CASL/PCASL-based methods, such as dynamic ASL (DASL) (11), Turbo-DASL (12), and PASL-based methods, such as Turbo-ASL (13) and Turbo-QUASAR (14). The PASL-based methods have the potential to reach the maximal labeling duty cycle and improved temporal resolution, which requires that the temporal widths of boluses are created to match the repetition time (TR), forming a seamless train of label/control throughout the ASL experiment. However, due to different flow velocities (15) and geometries of different feeding arteries, the temporal widths of the boluses with PASL are typically inhomogeneous across vessels. If the temporal width of a bolus is longer than the TR, the labeling duty cycle will be reduced due to shortened label from double inversion of some portion of the blood (if two labels are applied consecutively) or shortened control (if a control follows the label). If the temporal width of a bolus is shorter than the TR, the labeling duty cycle will be reduced because there will be some portion of delivered blood not contributing to the ASL signal. Both situations can happen in Turbo-ASL and Turbo-QUASAR. Methods such as QUIPSS II (16) and Q2TIPS (17) can be applied to create a uniform temporal width of boluses across vessels and produce quantitative measures of perfusion; however, the extra pulses saturate some portion of the delivered blood and take additional time, resulting in reduced labeling duty cycle and/or reduced temporal resolution.

To achieve the optimal labeling duty cycle, improved temporal resolution and quantitative measurement of CBF, we report here a novel labeling strategy developed to control the temporal widths of boluses in different vessels that can match the TR with a single labeling pulse. This method adds additional in-plane gradient pulses to existing slice-selective (SS) adiabatic full passage (AFP) pulses to induce a wedge-shaped (WS) inversion, creating different thicknesses at different vessels according to the flow velocities to create boluses of uniform temporal width. There are other 2-D radiofrequency (RF) pulses (18) capable of modulating the inversion thickness in space. However, these pulses typically require longer pulse duration and/or higher RF power than the proposed method. In comparison, the proposed WS inversion pulse is simple to implement and is capable of maintaining the same pulse duration, RF power and adiabatic properties of current SS AFP pulses.

Theory

In conventional SS AFP, a through-plane (Z) gradient pulse accompanies the RF pulse for slice-selection. the frequency of the AFP RF pulse moves from one side to the other within the frequency-swept range. In the presence of a gradient, the “on-resonance” frequency determines a plane in space where the magnetization is rapidly perturbed. With the Z gradient alone, the frequency sweeping and the movement of the “on-resonance” plane are identical across the X-Y plane, resulting in a constant inversion thickness in space.

To modify the shape/thickness of the inversion region across the X-Y plane, the movement of the “on-resonance” plane can be modulated by the combination of a conventional SS AFP and additional in-plane gradient pulses. Different shapes of the inversion region can be created by this means. In this study, a linear modulation on the inversion thickness at different in-plane positions was implemented, hence the name WS-SS inversion.

Following previous work, it is useful to view the dynamics of the magnetization in a frequency-modulated (FM) frame, defined as a frame of reference that rotates at the variable frequency of the RF pulse (19). In the FM frame the transverse component of the effective field is the RF field, $\boldsymbol{\omega_1}(t)$, along the $\hat{\boldsymbol{x}}'$ direction; it varies in amplitude but always lies along the same axis by the definition of the FM frame. The longitudinal component of the effective field along the $\hat{\boldsymbol{z}}'$ direction, $\boldsymbol{\Delta\omega}(t)$, is the total off-resonance term, the difference between the instantaneous RF frequency and the resonant frequency of the spins (19,20):

$$\boldsymbol{\omega_1}(t)=\gamma \cdot B_1^0 \cdot F_1(t)\hat{\boldsymbol{x}}', \quad [1]$$

$$\boldsymbol{\Delta\omega}(t)=[\Omega(\mathrm{t}) - A \cdot F_2(t)]\hat{\boldsymbol{z}}', \quad [2]$$

where γ is the gyromagnetic ratio, B_1^0 and A are the amplitudes of the RF field and the FM of the AFP pulse respectively, and $F_1(t)$ and $F_2(t)$ are normalized unit-less functions defining the shapes of the amplitude modulation (AM) and FM parts of the RF pulse respectively.

The first term in $\boldsymbol{\Delta\omega}(t)$ ($\Omega(t)$) is the resonant frequency offset generated by the gradient of the SS AFP pulse (Z gradient) and the chemical shift. The second term is due to the frequency modulation of the AFP pulse, $A \cdot F_2(t)$. If we express $\Omega(t)$ as a function of an amplitude and a shape function during the AFP, then

$$\Omega(t)=C \cdot F_3(t), \quad [3]$$

and

$$\boldsymbol{\Delta\omega}(t)=[C \cdot F_3(t) - A \cdot F_2(t)]\hat{z}', \quad [4]$$

where C and $F_3(t)$ are the amplitude and the normalized shape function of the frequency offset. At this point we neglect chemical shift effects and consider the resonant frequency to be determined just by the applied gradient. Specifically, we consider the case that the frequency offset is generated by the Z gradient applied during the AFP at position z, leading to:

$$C(z)=\gamma \cdot G_{z,A} \cdot z, \quad [5]$$

where $G_{Z,A}$ is the amplitude of the Z gradient. Now $F_3(t)$ is the shape of the Z gradient.

To modulate the inversion thickness in the X-Y plane (for simplicity, only the gradient along the X direction is considered), various gradient waveforms can be utilized. However, given a predesigned SS AFP pulse, it is desirable to maintain its adiabatic properties. To achieve this, an X gradient pulse can be added with its shape a combination of the FM and the Z gradient waveforms from the original AFP pulse:

$$G_x(t)=G_{x,A} \cdot [F_2(t) - \varepsilon \cdot F_3(t)], \quad [6]$$

where $G_{X,A}$ is the amplitude of the X gradient and ε is a unit-less factor that can shift the inversion region by a different distance along the Z direction at different X locations, i.e., shearing the inversion region along the Z direction.

At location(x, z), the frequency offset consists of both the frequency-offset term from the RF pulse and that induced by the applied gradient pulses, i.e., the Z and the X gradients. Adding the frequency offset induced by the X gradient into Eq. 4, now the combined FM function at location (x, z) is

$$\mathbf{\Delta\omega}(x,z,t)=[C(z)\cdot F_3(t)+\gamma\cdot x\cdot G_x(t)-A\cdot F_2(t)]\hat{\boldsymbol{z}}'=[C'(x,z)\cdot F_3(t)-A'\cdot F_2(t)]\hat{\boldsymbol{z}}', \quad [7]$$

Where

$$C'(x,z)=C(z)-\varepsilon\cdot\gamma\cdot G_{x,A}\cdot x=\gamma\cdot G_{z,A}\cdot\left(z-\varepsilon\cdot\frac{G_{x,A}}{G_{z,A}}\cdot x\right), \quad [8]$$

and

$$A'=A\cdot\left(1-\frac{\gamma\cdot G_{x,A}}{A}\cdot x\right). \quad [9]$$

Equation 8 indicates that the group of spins on resonance at time *t* was located at position *z* at all X positions before adding the X gradient, is now shifted to $\left[x, z-\varepsilon\cdot\frac{G_{x,A}}{G_{z,A}}\cdot x\right]$ after adding the X gradient. The shift distance is based on the position *x* and the factor ε, leading to the shear of the inversion region along the Z direction.

Equation 9 defines the new frequency-swept range (for simplicity, we assume $A'>0$ is satisfied), as a linear function of position *x*, and in turn the inversion thickness as a linear function of x. It is noted that at the pivot of $x=\frac{A}{\gamma\cdot G_{x,A}}$, $A'=0$; when $x>\frac{A}{\gamma\cdot G_{x,A}}$, the linear modulation on the thickness of the WS inversion pulses still holds, except that now the frequency-swept direction in space is reversed.

Now let us examine the adiabaticity, which is defined as the ratio of the rotation rate of spins about the effective magnetic field to the rate of the effective magnetic field orientation change. This ratio describes how well the spins follow the effective magnetic field as it changes in the pulse duration. Following the derivations in (20), for a group of spins at position *z* seeing the frequency offset of $|\Omega|<A$, the adiabatic condition is

$$K(\Omega,z,t)=\left|\frac{\gamma\cdot \mathrm{B}_{\mathrm{eff}}^{\Omega}(t)}{\dot{\alpha}}\right|=\frac{A^2}{\gamma\cdot B_1^0}\cdot\frac{\left[\left(\gamma\cdot B_1^0\cdot F_1(t)/A\right)^2+\left(F_2(t)-C(z)/A\cdot F_3(t)\right)^2\right]^{3/2}}{\left|\left(F_2(t)-C(z)/A\cdot F_3(t)\right)\cdot\dot{F}_1(t)-\left(\dot{F}_2(t)-C(z)/A\cdot\dot{F}_3(t)\right)\cdot F_1(t)\right|}\gg 1, \quad [10]$$

where $B_{\mathrm{eff}}^{\Omega}(t)$ is the effective magnetic field (the combination of the RF field $\boldsymbol{\omega}_1$ and the frequency offset $\mathbf{\Delta\omega}$ in the FM frame) seen by the group of spins and α' is the rate of change

of the $B_{\text{eff}}^{\Omega}(t)$ orientation in Hz, $F'_1(t)$, $F'_2(t)$and $F'_3(t)$ are the derivatives of $F_1(t)$, $F_2(t)$ and $F_3(t)$ respectively. With most reasonable choices for the AM and FM functions, the most critical time of the adiabatic condition is when the effective field is crossing the transverse plane ($t = t_\Omega$, i.e., on resonance) at position $z = z_\Omega$, that is,

$$C(z_\Omega) \cdot F_3(t_\Omega) - A \cdot F_2(t_\Omega) = 0. \quad [11]$$

Substitution of Eq. 11 into Eq. 10, it can be simplified to

$$K(t_\Omega) = \frac{(\gamma \cdot B_1^0 \cdot F_1(t_\Omega))^2}{A \cdot |\dot{F}_2(t_\Omega) - \frac{F_2(t_\Omega)}{F_3(t_\Omega)} \cdot \dot{F}_3(t_\Omega)|} \gg 1. \quad [12]$$

Similarly, with the X gradient added, at $t = t_\Omega$, the group of spins on resonance is located at $[x, z - \varepsilon \cdot \frac{G_{x,A}}{G_{z,A}} \cdot x]$. Substituting A and C with C' and A' accordingly into Eqs. 10 and 11, the new adiabaticity at location x is

$$K'(x, t_\Omega) = \frac{(\gamma \cdot B_1^0 \cdot F_1(t_\Omega))^2}{A' \cdot \left|\dot{F}_2(t_\Omega) - \frac{F_2(t_\Omega)}{F_3(t_\Omega)} \cdot \dot{F}_3(t_\Omega)\right|} = \frac{1}{|1 - \frac{\gamma \cdot G_{x,A}}{A} \cdot x|} K(t_\Omega). \quad [13]$$

Equation 13 states that the adiabaticity at the most critical time with the X gradient added is scaled by the inverse of a scaling factor, $|1 - \frac{\gamma \cdot G_{x,A}}{A} \cdot x|$, compared to that of the original SS AFP pulse. This scaling is applied uniformly along the Z direction at any given position x, so the shape of the spatial distribution of the adiabaticity along the Z direction is preserved except that it is expanded/squeezed along the Z direction accordingly. If the original SS AFP pulse is an Offset-Independent Adiabaticity (OIA) (19,20) pulse, the WS AFP pulse maintains the OIA property as well. Equation 13 is well maintained when $|\Omega| \ll A$, i.e., within the effective inversion band, and it provides increased adiabaticity as the thickness decreases. However, note that when A' decreases as the position x changes, the transition bands, in which the adiabatic condition degrades and the longitudinal magnetization transits from 1 to -1, close on the effective inversion region, resulting in smaller adiabaticity than that predicted by Eq. 13. This should not be a concern as long as the adiabaticity is still sufficiently high to generate efficient inversion. In general, given that the adiabatic condition is satisfied at the X position with the largest designated thickness, all other locations with smaller thicknesses (except when A' is comparable to the transition bandwidth) should have higher adiabaticity.

In applications such as PASL, it is typically desired to have the distal boundary of the inversion region parallel to the proximal boundary of the imaging region (axial imaging is

assumed). To do this, the offset factor ε can be calculated to set the X gradient to zero at the end of the pulse (i.e., $G_x(t_n) = 0$, where t_n is the last point of the pulse), so the on-resonance plane reaches the distal boundary of the inversion region at the end of the pulse.

By setting Eq. 6 to zero at t_n, the offset factor ε can be calculated:

$$\varepsilon = F_2(t_n)/F_3(t_n), \quad [14]$$

where $F_2(t_n)$ and $F_3(t_n)$ are the last points of the FM and the Z gradient waveforms of the original SS AFP pulse. In other words, the angles of the boundaries of the WS inversion region are given by $(\frac{G_x(t)}{G_z(t)})$ at $t = t_0$ and t_n: at $t = t_0$ the X gradient is nonzero, so the angle of the titled proximal boundary is $\arctan(\frac{G_x(t_0)}{G_z(t_0)})$; at $t = t_n$ the X gradient is zero, so the angle of the tilted distal boundary is zero and parallel to the proximal boundary of the imaging region. This can be seen in Figure 1d.

Note that rotating the additional gradients in plane (i.e., expanding G_x to G_{xy}) will rotate the WS inversion region in plane. This allows for individual control of the inversion thicknesses at up to three points in X-Y plane.

Methods

The WS inversion was implemented based on an SS HS inversion pulse with sech/tanh modulation (19) in amplitude and frequency accordingly and a constant Z gradient, which corresponds to a constant off resonance term $\Omega(t) = \Omega_c$. Following the theory above, the in-plane gradient in the WS inversion pulse takes the waveform of the FM in the HS pulse:

$$G_x(t) = G_A \cdot [\tanh(\beta t) - \varepsilon] \cdot, \quad [15]$$

where β is the truncation factor of the HS pulse. The performance of the WS inversion was examined through Bloch simulations and was compared with the conventional SS inversion in phantom experiments.

Simulations

The parameters of the HS pulse used in the simulation were: pulse duration = 15 ms, $\mu = 25$ rad/s, $\beta = 400$, temporal resolution = 4 μs, maximal $B_1 = 23$ μT and the amplitude of the RF pulse windowed by $\cos^{0.65}(t)$. The Z gradient was set to induce a nominal inversion thickness of 10 cm without the in-plane gradients. The WS inversion pulses using the in-plane gradient waveforms with $\varepsilon = 0$ and $\varepsilon = 1$ were simulated. The evolution of the longitudinal magnetization (M_z) within a 20 cm (X) by 20 cm (Z) space was observed during the WS pulses. To investigate the effect of the in-plane gradients on the adiabaticity, the adiabaticity during the WS pulses was calculated for both gradient conditions ($\varepsilon = 0$ and

$\varepsilon = 1$). To demonstrate the effect of insufficient B_1, the M_z after the application of the WS inversion pulses was also simulated with a maximal $B_1 = 15$ μT. The relaxation effects were ignored in the simulations.

Phantom Experiments

The WS inversion pulse was implemented on a 3-Tesla GE scanner (Discovery MR750; GE Healthcare, Waukesha, WI) with the same parameters as described in the simulations. The images were acquired with an 8-channel receive-only head coil and were complex-reconstructed offline with an in-house developed program.

Stationary phantom

The WS inversion pulse was compared with a conventional SS inversion pulse on a stationary gel phantom. The inversion pulses were applied to generate inversion regions along the S/I direction. The inversion thicknesses were set to 4 cm for the conventional SS inversion, and 4 cm at the center and 5 cm at 2 cm on the left for the WS inversion. Coronal images were acquired immediately after the labeling (inversion time (TI) = 20 ms) to measure the inversion profiles (label). Control images were also collected as in the PICORE method (9) without the Z and X gradients. Other imaging parameters included: field of view (FOV) = 220 × 220 mm, image matrix = 64 × 64, slice thickness = 6 mm, spin echo with spiral readout, TR/echo time (TE) = 2 s/10.4 ms, 2 pairs of label/control after 2 dummy repetitions.

The label and control images were averaged through repetitions. A mask based on the magnitude of the MR signal was applied to remove the noisy pixels outside the phantom. The longitudinal magnetization measured under the label condition was projected onto and normalized to that measured under the control condition. The imaginary part was considered as noise and then discarded. The profiles of the normalized longitudinal magnetization at the center and 2 cm away on both sides were examined. The full widths at half maximum (FWHMs) were calculated from the profiles to measure the inversion thicknesses at these locations.

Flow phantom

The feasibility of controlling the temporal bolus width in PASL using WS inversion pulse was tested in a flow phantom. The flow phantom consisted of three plastic tubes (“vessels”) running parallel on the surface of a cylindrical bottle to simulate three supplying arteries in a PASL experiment. Tap water was running in the phantom driven by a water pump. The phantom was placed in the scanner with the flow along the S/I direction and the in-plane locations of the “vessels” arbitrary. The resistance in each “vessel” was adjusted to generate different flow velocities from each other. A cross-section of the flow phantom can be seen in Figures 4a and b, where the unlabeled “vessel” had the returning flow.

An inversion thickness of 4 cm was used with the conventional SS inversion. Images were collected 1 cm downstream from the inversion region. In order to capture the shape of the label bolus, 60 images were acquired every 28.9 ms, starting at 20 ms and up to 1726 ms after the application of the inversion pulse. Other imaging parameters were: FOV = 100 ×

100 mm, image matrix acquired at 48 × 48 and reconstructed to 64 × 64, slice thickness = 3 mm, gradient echo with spiral readout, TR/TE = 4 s/3.8 ms, 10 pairs of label/control after 4 dummy repetitions.

Phase-contrast images were acquired at the distal boundary of the inversion region to provide estimates of the flow velocities in the labeling region with FOV = 100 × 100 mm, reconstructed matrix size = 256 × 256, slice thickness = 3 mm and VENC = 20 cm/s (along the S/I direction). According to the average velocities in the three “vessels”, the inversion thicknesses were set to 4.0 cm, 3.0 cm and 1.9 cm for “vessels” 1, 2 and 3 (V1, V2 and V3 shown in Figs. 4a and b) respectively to yield similar temporal widths of boluses with the WS inversion pulse. Other imaging parameters were kept the same as in the conventional SS inversion experiment.

To correct for T_1 relaxation, a series of inversion recovery images of the tap water staying stationary in the phantom were collected at TIs = 25, 50, 100, 200, 400, 800, 1600, 2400, 3200 and 4800 ms. The measured T_1 of the tap water was 3.0 s and was applied in the temporal width of bolus analysis.

The label and control images were averaged and normalized as described in the stationary phantom data processing. The normalized signal difference was calculated from subtraction of the label from the control. Small regions of interest (ROIs) were picked at the center of each of the “vessels”. Normalized signals were averaged within these ROIs and plotted against time as the measure of the shapes of the boluses after T_1 correction. The FWHM of each profile was estimated as the measure of the temporal width of the bolus.

Human Experiments

To demonstrate the feasibility of applying the WS inversion pulse to control the temporal width of the boluses in vivo, a young healthy male subject (age 22) was scanned under an IRB approved protocol on the same scanner as in the phantom experiments. An angiogram was collected to determine the locations of the main feeding arteries, the labeling regions and the imaging planes. To test the performance of the WS inversion pulse in the presence of four feeding arteries (left and right internal carotid and vertebral arteries, LICA, RICA, LVA and RVA respectively), the imaging plane was chosen so that all the four feeding arteries were visible where the ASL signals could be measured. For experimental simplicity, cine phase-contrast images were acquired at the imaging plane with FOV = 200 × 200 mm, reconstructed matrix size = 256 × 256, slice thickness = 3 mm, VENC = 60 cm/s (along the S/I direction) and 16 cardiac phases. The averaged velocity was calculated across cardiac phases in each artery.

The conventional SS inversion was applied with an inversion thickness of 15 cm and a 2 cm gap between the labeling region and the imaging plane. Sixty images were acquired every 30.4 ms, starting at 25 ms and up to 1819 ms after the application of the inversion pulse. Other imaging parameters were: FOV = 200 × 200 mm, image matrix acquired at and reconstructed to 128 × 128, slice thickness = 3 mm, gradient echo with four-interleaved spiral readout, TR/TE = 3 s/7.3 ms, flow compensation in the excitation and imaging pulses, 10 pairs of label/control after 4 dummy repetitions. For the WS inversion pulse, the

inversion thicknesses were set to 15 cm, 13 cm and 9 cm at the RICA, LICA and the middle point (as an approximation) of the LVA and the RVA respectively. Other imaging parameters were kept the same as in the conventional SS inversion experiment.

The data processing of the human experiments followed that in the flow phantom experiments, except that an assumed T_1 of 1.66 s (21) was used for T_1 correction.

Results

Simulations

The evolution of the M_z and the movement of the "on-resonance" plane during the WS inversion pulse are shown in Figures 1c and d for WS inversion with $\varepsilon = 0$ and $\varepsilon = 1$ respectively (Figs. 1a and b). The final M_z after application of WS inversion at $B_1 = 23$ μT is shown in Figures 1e and f. With $\varepsilon = 1$, the inversion at different X locations was shifted and a horizontal distal boundary was created as expected. The M_z profiles at three X locations were shown in Figures 1g and h, with the corresponding locations color-coded as depicted in Figures 1e and f. One can see that uniform inversion was achieved within the designated WS regions at $B_1 = 23$ μT, when the adiabatic condition was well met. At $B_1 = 15$ μT, the inversion at the thickest location among the three was slightly degraded, however, the inversion with smaller inversion thicknesses designated at the other two locations was not affected, as predicted in the theory section. The minimal adiabaticity maps during the pulses are shown in Figures 2a and b, with the profiles at three locations shown in Figures 1c and d. In case of insufficient B_1, the overall adiabaticity will be reduced. The regions close to the boundaries are more sensitive to B_1 reduction, where the adiabaticity may fall below the adiabatic threshold first, resulting in incomplete inversion, as shown with $B_1 = 15$ μT here. However, as pointed out in the theory section, as long as the adiabatic condition is satisfied at the location with the largest inversion thickness, all other locations should have higher adiabaticity (Figs. 2c and d) and therefore more robust inversion. The maps of minimal adiabaticity also show the shift at different X locations as the offset factor ε changed from 0 to 1.

Phantom Experiments

Stationary phantom—The normalized M_z maps using the conventional SS and the WS inversion pulses are shown in Figure 3a, with the inversion profiles at the middle and 2 cm away on both sides shown in Figure 3b. The FWHMs of the inversion thicknesses were 3.9 cm, 4.0 cm and 4.0 cm with the conventional SS inversion, and 3.0 cm, 4.0 cm and 5.0 cm with the WS inversion at the locations depicted with blue, green and red lines respectively. The WS inversion pulse worked as expected. Relatively uniform inversion was achieved within the inversion regions with both pulses.

Flow phantom—A cross-sectional image and a velocity map of the flow phantom at the distal boundary of the inversion region are shown in Figures 4a and b respectively. The averaged velocities were 7.1 cm/s, 5.4 cm/s and 3.4 cm/s in V1, V2 and V3 respectively. The averaged signal difference between the label and the control conditions at different TI times after T_1 correction was shown in Figure 4c. The delays of the label arrival were the same in

the same “vessel” between the conventional SS inversion and the WS inversion, and were measured as 0.10 s, 0.15 s and 0.24 s in V1, V2 and V3 respectively. Given the 1 cm gap between the inversion and the imaging regions, these delays corresponded to velocities of 10.0 cm/s, 6.7 cm/s and 4.2 cm/s, and matched well with the highest velocities at the centers of the “vessels” shown in Figure 4b. This indicates that the WS inversion pulse was able to generate the same flat distal boundary as the conventional inversion pulse did, therefore leaving the transit delays unchanged as using the conventional SS inversion labeling.

For the conventional SS inversion, the FWHMs were measured as 0.53 s, 0.74 s and 1.04 s. For the WS inversion, the FWHMs were 0.53 s, 0.52 s and 0.52 s. Compared to the conventional SS inversion pulse, the WS inversion pulse was able to control and generate a uniform temporal width in these “vessels” with different velocities. This clearly demonstrates the feasibility of using the WS inversion pulse to independently control the inversion thicknesses and the temporal widths of boluses at up to three in-plane locations as expected.

Human Experiments

An image of averaged ASL signals and a velocity map at the imaging plane are shown in Figures 5a and b respectively. The averaged velocities were 14.7 cm/s, 17.9 cm/s, 11.9 cm/s and 7.5 cm/s in RICA, LICA, LVA and RVA respectively. The averaged ASL signals at different TIs after T_1 correction are shown in Figure 5c. The results showed similar patterns as in the flow phantom experiments. The delays of the label arrival in the arteries were unchanged between the conventional SS inversion and the WS inversion, except that the ASL signal arose slightly earlier in the RICA with the WS inversion. Nevertheless, the arrival times for the majority of the label (measured from the main upslope) remained almost unchanged as expected and were measured as 0.13 s, 0.05 s, 0.21 s and 0.27 s with the conventional SS inversion and 0.14 s, 0.05 s, 0.21 s and 0.28 s in RICA, LICA, LVA and RVA respectively.

For the conventional SS inversion, the FWHMs were measured as 0.75 s, 0.78 s, 0.99 s and 1.12 s. For the WS inversion, the FWHMs were 0.75 s, 0.73 s, 0.58 s and 0.69 s. Compared to the conventional SS inversion pulse, the WS inversion pulse was able to reduce the temporal widths of the boluses in both vertebral arteries to largely match that in the ICAs, generating a relatively uniform temporal width in four feeding arteries with different velocities. However, due to the simple approximation of using the averaged velocity and the middle point of the two vertebral arteries for the third point to define the WS inversion, the temporal width of the bolus in the LVA was slightly shorter than desired. This may be improved by adjusting the inversion thickness and the location of the third point in the prescription.

Discussion

In this study, we had demonstrated that by adding X-Y gradients in a conventional SS HS inversion pulse with a constant Z gradient, the shape of the inversion region could be altered from a slab to a wedge, resulting in different inversion thicknesses at different locations. As shown in the theory section, the inversion thickness at different X-Y location is independent

of the shape of the Z gradient applied with the SS AFP. This means the same principle is applicable with other types of SS AFP inversion pulses with non-constant Z gradient, such as VERSE transformed SS AFP (22), frequency offset corrected inversion (FOCI) (23), gradient-modulated offset-independent adiabaticity (GOIA) (20), etc. This was confirmed by Bloch simulations (results not shown here). For simplicity, the offset induced by chemical shift was not taken into account in this study; however, its influence can be assessed by incorporation of this term into Eqs. 3 and 4, and follow the derivations thereafter.

As shown in the theory section, given an SS AFP pulse, the adiabaticity at the most critical time decreases as the intended inversion thickness increases, so the largest inversion thickness with sufficient efficiency is limited by the properties of the original SS AFP pulse. As long as the adiabatic condition is maintained where the largest thickness is requested, efficient inversion should be achieved within the whole region of interest, except for the locations where the inversion thickness is close to zero. If the inversion thickness is too large at some locations, the inversion efficiency reduces first in regions with relatively low adiabaticity. For example, with an SS AFP pulse with relatively uniform adiabaticity along Z, such as OIA pulses, the efficiency reduction will be relatively uniform along Z. With the cosine-windowed SS HS pulse in the simulation, the efficiency reduces first in regions around the boundaries as shown in Figures 1g and h.

The shape of the X-Y gradients resembles that of the frequency-swept function (or the combination with the Z gradient if shearing the inversion region is required) of the original AFP pulse to maintain the adiabatic properties. But unlike the FM (typically implemented as phase modulation), the gradient pulses are subject to hardware limitations such as slew rate. It should be kept in mind that if the added X-Y gradient waveform cannot follow the designated shape given by Eq. 6 due to hardware limitation/imperfection, the pulse would need to be modified to satisfy the constraints. However, under typical circumstances this is unlikely to pose a significant limitation. In the example in the simulation above, the peak gradient and slew rate were 0.372 mT/m and 0.15 T/m/s.

The additional in-plane gradient pulses can be applied in PASL methods, such as EPISTAR (7), FAIR (8), PICORE (9) and their modifications, under the label condition. To obtain the control images with magnetization transfer effect compensation, the additional in-plane gradient pulses can simply be turned off. However, if eddy current effects limit one to use EPISTAR, the same additional in-plane gradients can be applied under the control condition to keep the gradient pulses identical under both label and control conditions (9).

In the flow phantom experiments, it was demonstrated that the WS inversion region can be rotated in plane to generate three different inversion thicknesses to match the flow velocities at different locations, therefore controlling the temporal widths of boluses in PASL experiments. This should be sufficient for perfusion measurement in brain, where left and right internal carotid and the vertebrobasilar arteries are the main feeding arteries. In practice, because of the tortuosity of the feeding arteries, in order to control the temporal widths of boluses accurately, the velocities and the lengths of the feeding arteries in the inversion region should be measured and the inversion thicknesses should be assigned accordingly. Given a typical location and a thickness of the inversion region in PASL

experiments, the proximal boundary of the inversion region is likely to land on the vertebral arteries, requiring individual control of inversion thicknesses at four locations, as we had tested and demonstrated in the human experiments. As an approximation, the location of the middle point and the averaged velocity of the two vertebral arteries can be used. This could result in compromised accuracy on the control of the temporal widths of the boluses in vertebral arteries as shown in the human experiments. However, given relatively low and likely similar velocities in the vertebral arteries compared to that in the carotid arteries, this effect may not be significant. In addition, adjustment of the inversion thickness and the location to prescribe the WS inversion region can be used to minimize the inaccuracy. This requires further study to examine its feasibility.

The WS inversion pulse is capable of handling relatively small spatial separations between vessels, e.g., between the carotid and the vertebrobasilar arteries. For example, if the desired inversion thicknesses are 15 cm and 7.5 cm in the carotid and the vertebrobasilar arteries, respectively, (assuming a velocity ratio of 2:1), a small spatial separation of 1 cm between them along the anterior/posterior (A/P) direction will require the peak A/P gradient to be 3.72 mT/m. This is well within the capability of a typical scanner.

Note that due to the small size of the flow phantom, the velocities were chosen to be low to generate relatively long temporal widths of boluses for minimizing potential inaccuracy in the temporal width measurements. For high velocities in vivo, the inversion thicknesses can be linearly scaled up to match the velocities. This scaling will not affect the performance of the pulse, as demonstrated in the human experiments.

With the temporal width of the bolus in each vessel under control, PASL labeling can be performed more rapidly and reach the optimal temporal labeling duty cycle. As mentioned in the Introduction section, the temporal widths of the boluses can be set to match the TR, so that the labeling process (label/control) can be applied to the arterial blood continuously and seamlessly. This way, all the arterial blood is contributing to the ASL signal during the PASL experiment. In addition, the temporal widths of the boluses are known, so quantitative estimates of perfusion can be acquired.

The temporal resolution of the PASL experiment can be significantly improved with rapid labeling and imaging. However, because the arterial blood under the label and the control conditions contributes to the MR signal in opposite directions, in practice, one may allow a small number of labels/controls to be applied consecutively for the ASL signal to accumulate in the tissue, improving the SNR in each measurement. This will reduce the temporal resolution gain for each independent ASL measurement (a complete label/control cycle), but may still provide higher temporal resolution than that currently available, in addition to improvement of the SNR efficiency.

The WS inversion pulse is capable of keeping the distal boundary of the inversion region at the same location as with the SS inversion pulse, so the transit delays will remain unchanged, as demonstrated with the results from the flow phantom and the human experiments. The transit delay can be modeled and estimated from the ASL signal to produce quantitative estimates of perfusion.

Conclusions

A novel method to control the inversion thicknesses at different in-plane positions while maintaining the adiabatic properties of the original SS AFP pulses has been developed. A WS inversion pulse has been implemented based on an SS HS pulse and additional in-plane gradient pulses. It is demonstrated through Bloch simulations, phantom and human experiments to be capable of controlling the temporal widths of the boluses in vessels with different flow velocities. It should maximize the labeling duty cycle and improve the SNR efficiency and the temporal resolution in PASL experiments.

Acknowledgments

This work was funded by NIH-NS036722.

References

1. Deibler AR, Pollock JM, Kraft RA, Tan H, Burdette JH, Maldjian JA. Arterial Spin-Labeling in Routine Clinical Practice, Part 1: Technique and Artifacts. Am J Neuroradiol. 2008; 29(7):1228–1234. [PubMed: 18372417]
2. Alsop DC, Detre JA, Golay X, Gunther M, Hendrikse J, Hernandez-Garcia L, Lu H, Macintosh BJ, Parkes LM, Smits M, van Osch MJ, Wang DJ, Wong EC, Zaharchuk G. Recommended implementation of arterial spin-labeled perfusion MRI for clinical applications: A consensus of the ISMRM perfusion study group and the European consortium for ASL in dementia. Magn Reson Med. 2015; 73:102–116. [PubMed: 24715426]
3. Guo J, Wong EC. Increased SNR Efficiency in Velocity Selective Arterial Spin Labeling using Multiple Velocity Selective Saturation Modules (mm-VSASL). Magn Reson Med. 2014; doi: 10.1002/mrm.25462.
4. Kwong KK, Belliveau JW, Chesler DA, Goldberg IE, Weisskoff RM, Poncelet BP, Kennedy DN, Hoppel BE, Cohen MS, Turner R, Cheng HM, Brady TJ, Rosen BR. Dynamic magnetic resonance imaging of human brain activity during primary sensory stimulation. Proc Natl Acad Sci USA. 1992; 89:5675–5679. [PubMed: 1608978]
5. Williams DS, Detre JA, Leigh JS, Koretsky AP. Magnetic resonance imaging of perfusion using spin inversion of arterial water. Proc Natl Acad Sci U S A. 1992; 89(1):212–216. [PubMed: 1729691]
6. Dai WY, Garcia D, de Bazelaire C, Alsop DC. Continuous Flow-Driven Inversion for Arterial Spin Labeling Using Pulsed Radio Frequency and Gradient Fields. Magn Reson Med. 2008; 60(6):1488–1497. [PubMed: 19025913]
7. Edelman RR, Siewert B, Darby DG, Thangaraj V, Nobre AC, Mesulam MM, Warach S. Qualitative mapping of cerebral blood flow and functional localization with echo-planar MR imaging and signal targeting with alternating radio frequency. Radiology. 1994; 192(2):513–520. [PubMed: 8029425]
8. Kim SG. Quantification of relative cerebral blood flow change by flow-sensitive alternating inversion recovery (FAIR) technique: application to functional mapping. Magn Reson Med. 1995; 34(3):293–301. [PubMed: 7500865]
9. Wong EC, Buxton RB, Frank LR. Implementation of quantitative perfusion imaging techniques for functional brain mapping using pulsed arterial spin labeling. NMR Biomed. 1997; 10(4-5):237–249. [PubMed: 9430354]
10. Golay X, Stuber M, Pruessmann KP, Meier D, Boesiger P. Transfer insensitive labeling technique (TILT): application to multislice functional perfusion imaging. J Magn Reson Imaging. 1999; 9(3): 454–461. [PubMed: 10194717]
11. Barbier EL, Silva AC, Kim HJ, Williams DS, Koretsky AP. Perfusion analysis using dynamic arterial spin labeling (DASL). Magn Reson Med. 1999; 41(2):299–308. [PubMed: 10080277]
12. Meng Y, Wang P, Kim SG. Simultaneous measurement of cerebral blood flow and transit time with turbo dynamic arterial spin labeling (Turbo-DASL): application to functional studies. Magn Reson Med. 2012; 68(3):762–771. [PubMed: 22162211]

13. Wong EC, Luh WM, Liu TT. Turbo ASL: Arterial spin labeling with higher SNR and temporal resolution. Magn Reson Med. 2000; 44(4):511–515. [PubMed: 11025504]
14. Petersen, ET.; De Vis, JB.; van den Berg, CAT.; Hendrikse, J. Turbo-QUASAR: a signal-to-noise optimal arterial spin labeling and sampling strategy. Proceedings of the 21 th Annual Meeting of ISMRM; Salt Lake City, Utah, USA. 2013. p. 2146
15. Yazici B, Erdogmus B, Tugay A. Cerebral blood flow measurements of the extracranial carotid and vertebral arteries with Doppler ultrasonography in healthy adults. Diagn Interv Radiol (Ank). 2005; 11(4):195–198.
16. Wong EC, Buxton RB, Frank LR. Quantitative imaging of perfusion using a single subtraction (QUIPSS and QUIPSS II). Magn Reson Med. 1998; 39(5):702–708. [PubMed: 9581600]
17. Luh WM, Wong EC, Bandettini PA, Hyde JS. QUIPSS II with thin-slice TI1 periodic saturation: a method for improving accuracy of quantitative perfusion imaging using pulsed arterial spin labeling. Magn Reson Med. 1999; 41(6):1246–1254. [PubMed: 10371458]
18. Conolly S, Pauly J, Nishimura D, Macovski A. Two-dimensional selective adiabatic pulses. Magn Reson Med. 1992; 24(2):302–313. [PubMed: 1569869]
19. Garwood M, DelaBarre L. The return of the frequency sweep: Designing adiabatic pulses for contemporary NMR. J Magn Reson. 2001; 153(2):155–177. [PubMed: 11740891]
20. Tannus A, Garwood M. Adiabatic pulses. NMR Biomed. 1997; 10(8):423–434. [PubMed: 9542739]
21. Lu H, Clingman C, Golay X, van Zijl PC. Determining the longitudinal relaxation time (T1) of blood at 3.0 Tesla. Magn Reson Med. 2004; 52(3):679–682. [PubMed: 15334591]
22. Conolly S, Nishimura D, Macovski A, Glover G. Variable-Rate Selective Excitation. J Magn Reson. 1988; 78(3):440–458.
23. Ordidge RJ, Wylezinska M, Hugg JW, Butterworth E, Franconi F. Frequency offset corrected inversion (FOCI) pulses for use in localized spectroscopy. Magn Reson Med. 1996; 36(4):562–566. [PubMed: 8892208]

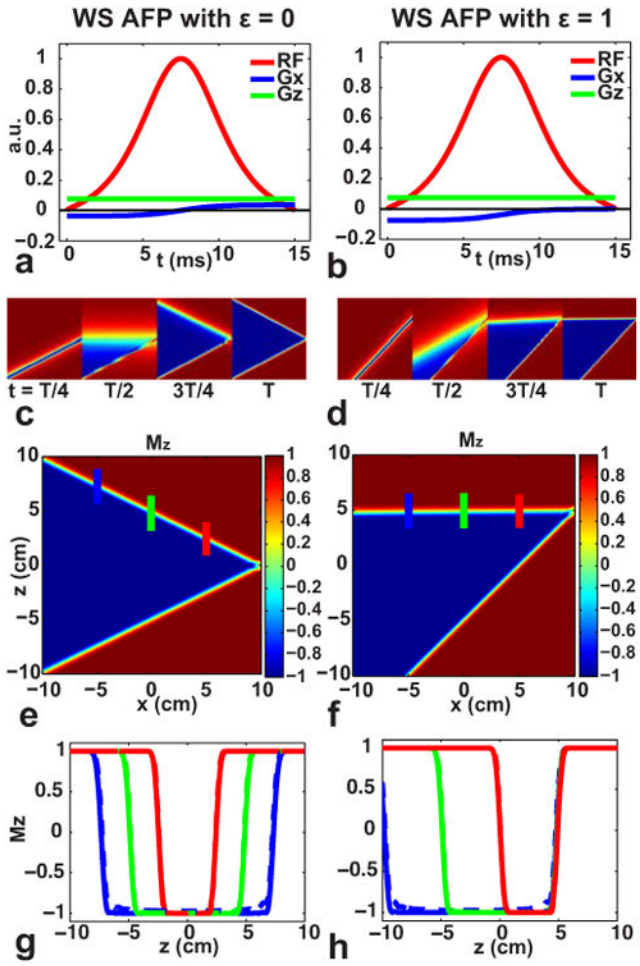

Figure 1.

The diagrams and results from Bloch simulations of the WS SS AFP pulses. (a), (c), (e), (g) and (b), (d), (f), (h) are from the WS AFP pulses with the offset factor $\varepsilon = 0$ and $\varepsilon = 1$ accordingly. (a), (b): the RF amplitude (red) and the X (blue) and Z (green) gradients of the WS inversion pulses; (c), (d): the evolution of the M_z during the WS inversion, showing the movement of the "on-resonance" plane, where T is the duration of the pulse; (e), (f): the final longitudinal magnetization M_z after application of the WS inversion pulses; (g), (h) the M_z profile at the locations indicated with colored stripes shown in (e) and (f), the solid and dashed lines represent the results simulated at B_1 levels of 23 μT and 15 μT.

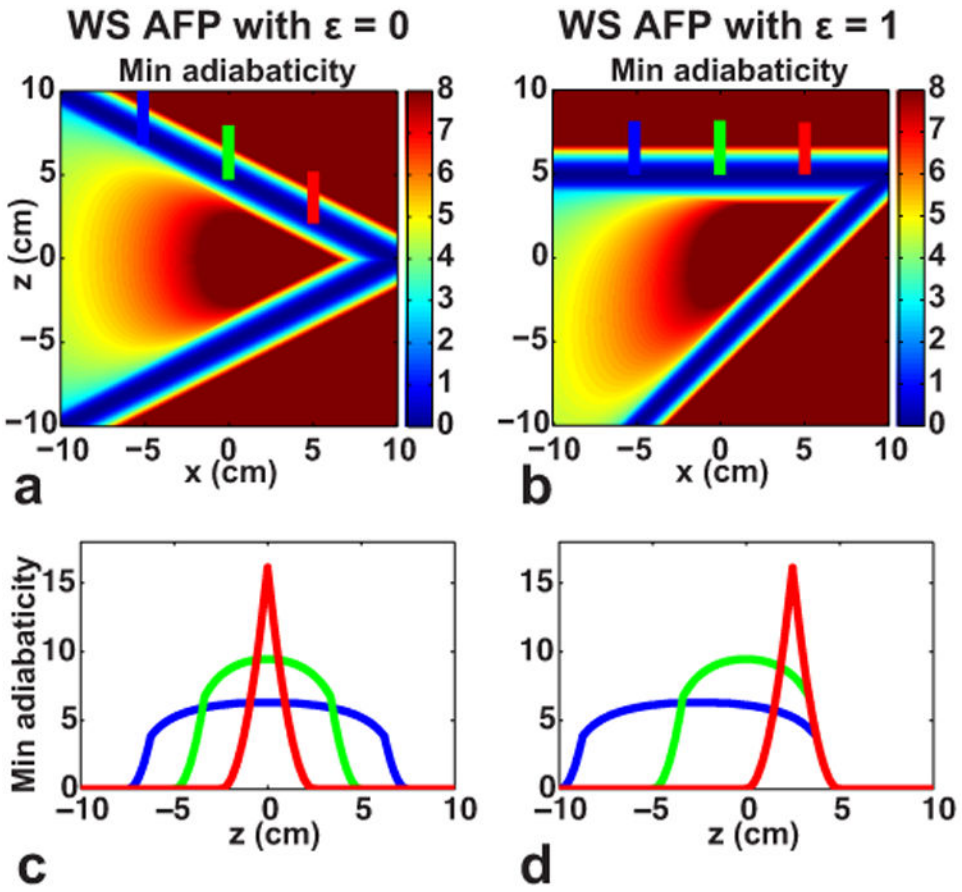

Figure 2.

The minimal adiabaticity maps of the WS SS AFP pulses. (a), (c) and (b), (d) correspond to the WS AFP pulses with the offset factor $\varepsilon = 0$ and $\varepsilon = 1$ showing in Figures 1a and b accordingly. (a), (b): the maps of the minimal adiabaticity during the WS inversion pulses; (c), (d): the profiles of the minimal adiabaticity within the inversion regions at locations indicated with colored stripes shown in (a) and (b) respectively; the maps of the minimal adiabaticity are capped at 8 for better visualization.

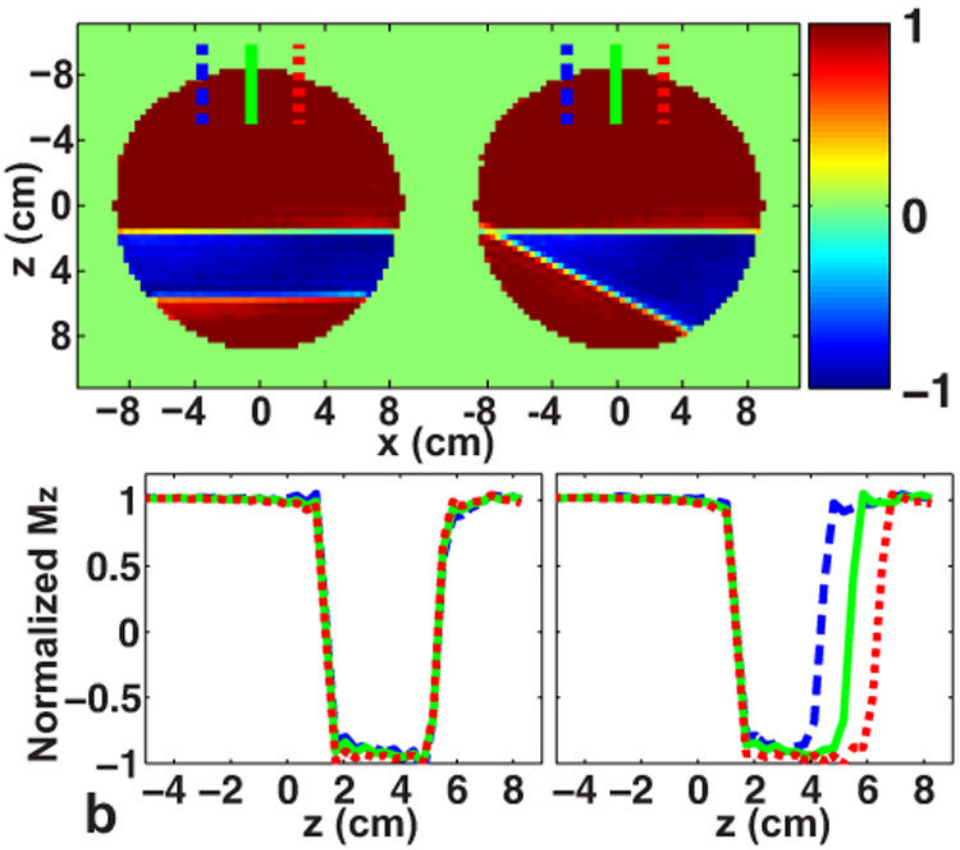

Figure 3.

(a) Normalized M_z maps after application of the conventional SS and the WS inversion pulses; (b) the M_z profiles within the phantom at the locations indicated with colored dashed, solid and dotted lines respectively, shown in (a).

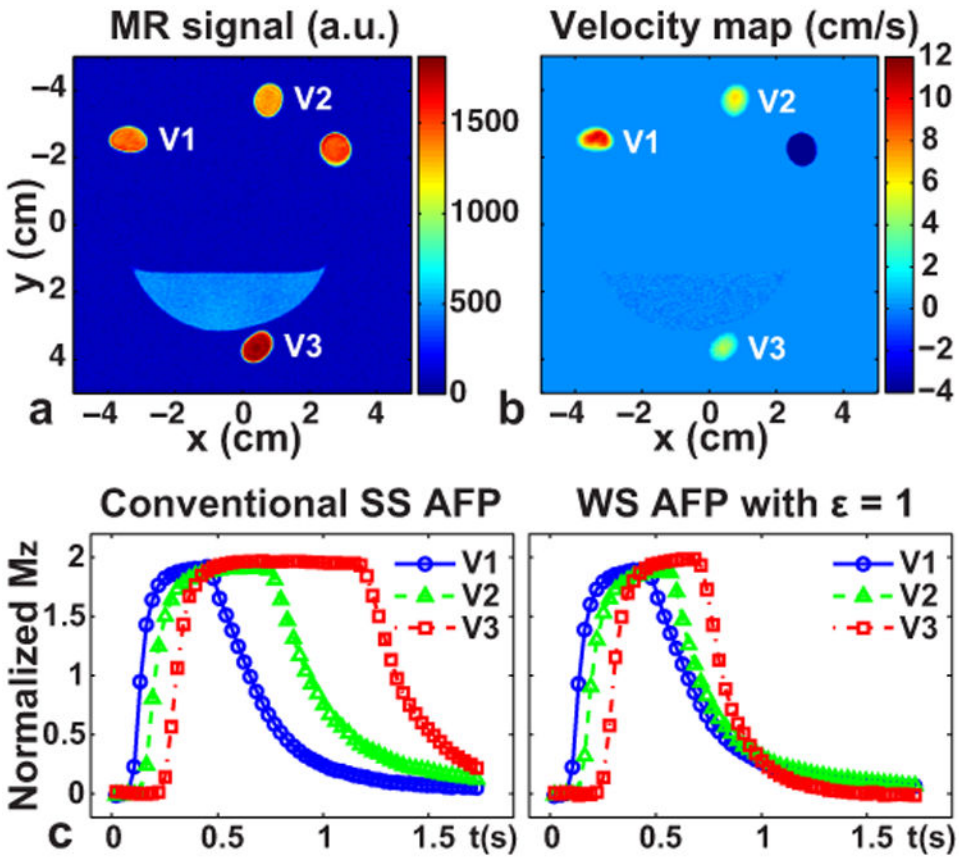

Figure 4.

(a) and (b): A cross-sectional image and a velocity map acquired at the distal boundary of the inversion region and the "vessel" labels, the returning flow velocities (negative values) were capped at -4 cm/s for a better visualization of the positive flows of interest; (c) normalized (control – tag) signal in each "vessel" after T_1 correction, acquired with conventional SS AFP and WS AFP inversion pulses (left and right respectively). It is clearly seen with WS AFP inversion pulses, the temporal width of bolus in each "vessel" was under control and well matched to each other.

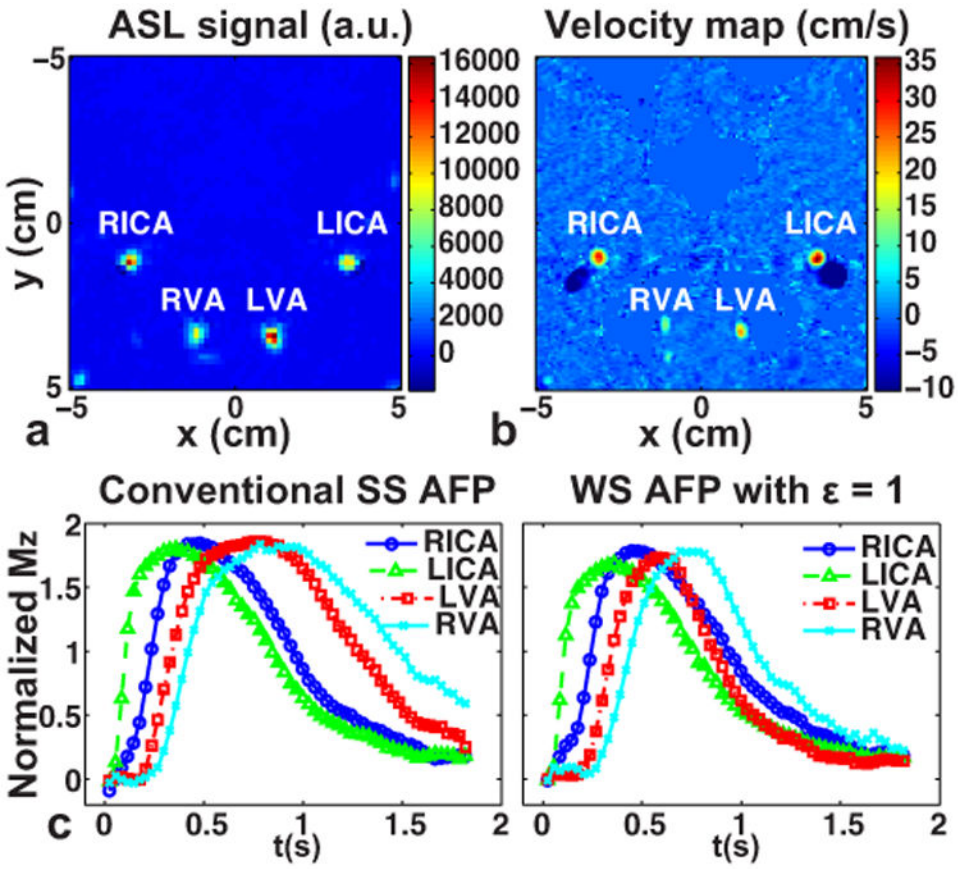

Figure 5.

(a) and (b): Zoomed-in images of averaged ASL signals and velocity map acquired at 2 cm distal from the inversion region in the human subject, with the arteries of interest labeled. The venous flow velocities (negative values) were capped at -10 cm/s for a better visualization of the positive flows of interest. (c) Normalized ASL (control – tag) signal in each artery after T_1 correction, acquired with conventional SS AFP and WS AFP inversion pulses (left and right respectively). Note that with WS AFP inversion pulses, the temporal widths of boluses can be controlled and matched to each other.